

# The new $P$ -chalcopyrite compound $\text{Cu}_2\text{FeIn}_2\text{Se}_5$ ; synthesis, thermal analysis, and crystal structure analysis by X-ray powder diffraction

G. E. Delgado<sup>a,f</sup>, P. Grima-Gallardo<sup>b,c</sup>, J. A. Aitken<sup>d</sup>, A. Cárdenas<sup>e</sup>, and I. Brito<sup>f</sup>

<sup>a</sup>Laboratorio de Cristalografía, Departamento de Química, Facultad de Ciencias, Universidad de Los Andes, Mérida 5101, Venezuela  
e-mail: gerzon@ula.ve

<sup>b</sup>Centro de Estudios de Semiconductores, Departamento de Física, Facultad de Ciencias, Universidad de Los Andes, Mérida 5101, Venezuela.

<sup>c</sup>Centro Nacional de Tecnologías Ópticas y Centro de Investigaciones de Astronomía, Mérida 5101, Venezuela.

<sup>d</sup>Department of Chemistry and Biochemistry, Duquesne University, Pittsburgh, Pennsylvania 15282, United States.

<sup>e</sup>Departamento de Física, Facultad de Ciencias Básicas, Universidad de Antofagasta, Campus Coloso, Antofagasta 1240000, Chile.

<sup>f</sup>Departamento de Química, Facultad de Ciencias Básicas, Universidad de Antofagasta, Campus Coloso, Antofagasta 1240000, Chile.

Received 6 October 2020; accepted 20 October 2020

The  $\text{Cu}_2\text{FeIn}_2\text{Se}_5$  alloy, belonging to the system  $(\text{CuInSe}_2)_{1-x}(\text{FeSe})_x$  with  $x = 1/3$ , was synthesized by the melt and annealing technique. The differential thermal analysis (DTA) indicates that this compound melts at 1017 K. The crystal structure of this new quaternary compound was established using powder X-ray diffraction. Cation distribution analysis indicates that this material crystallizes in a  $P$ -chalcopyrite structure, space group  $P\bar{4}2c$  ( $N^\circ 112$ ), with unit cell parameters  $a = 6.1852(2)$  Å,  $c = 12.3633(9)$  Å,  $V = 472.98(4)$  Å<sup>3</sup>.  $\text{Cu}_2\text{FeIn}_2\text{Se}_5$  is a new adamantane type compound derivative of the sphalerite structure, and consists of a three-dimensional arrangement of distorted  $\text{CuSe}_4$ ,  $\text{FeSe}_4$ , and  $\text{InSe}_4$  tetrahedral connected by common faces.

**Keywords:** Crystal structure; X-ray powder diffraction; Rietveld refinement;  $P$ -chalcopyrite; chemical synthesis; differential thermal analysis;  $\text{CuInSe}_2$ ; semiconductor

PACS: 61.05.cp; 61.50.Nw; 61.66.Fn; 61.40.b

DOI: <https://doi.org/10.31349/RevMexFis.67.18>

## 1. Introduction

The chalcopyrite family of compounds, with formula I-III- $\text{VI}_2$  (I= Cu, Ag, III= Al, Ga, In, VI= S, Se, Te) form an extensive group of semiconductor materials with diverse optical and electrical properties [1-3]. From the structural point of view, chalcopyrite crystallizes with tetragonal symmetry in the space group  $I\bar{4}2d$  ( $N^\circ 122$ ) being isostructural with the  $\text{CuFeS}_2$  mineral from which they take their name [4].

The addition of a II-VI binary compound (II= V, Mn, Fe, Co, Ni, Zn, Cd) to chalcopyrite produces alloys of composition (I-III- $\text{VI}_2$ )<sub>1-x</sub>(II-VI)<sub>x</sub>, and changing the composition variable  $x$ , it is possible to find the following compounds in this system: I<sub>2</sub>-II-III<sub>2</sub>- $\text{VI}_5$  ( $x = 1/3$ ), I-II-III- $\text{VI}_3$  ( $x = 1/2$ ), and I-II<sub>2</sub>-III- $\text{VI}_4$  ( $x = 2/3$ ), among others. These families of compounds fulfill the rules of formation of adamantane compounds and belong to the normal semiconductor compound families [5]. According to these rules, the cation substitution is carried out in such a way that an average number of four valence electrons per atomic site is maintained and in turn value of eight for the ratio between valence electrons to anions. Adamantane compounds are binary, ternary, or quaternary normal tetrahedral structure compounds that are

closely related to either cubic or hexagonal diamond [5]. In our laboratories, we have been studying these type of alloys from its synthesis, thermal and magnetic properties as well as their crystal structures [6-13]. Due to the great variety of possible compositions, these materials can be useful for applications such as tunable semiconductors [14], photovoltaics [15], non-linear optics [16], thermoelectrics [17], and particularly as spintronic device [18] due to the discovery of room-temperature ferromagnetism and super-paramagnetism in some of these materials [19].

In particular, the ternary chalcopyrite semiconductor  $\text{CuInSe}_2$  is one of the most studied materials due to its high optical absorption coefficient ( $\alpha \sim 104$  cm<sup>-1</sup> at 1 eV), which is essential for thin films photovoltaic applications. It crystallizes in an ordered structure, and melts congruently at 1259 K with an order-disorder thermal transition at 1083 K [20]. The addition to the ternary  $\text{CuInSe}_2$  of a metal transition element, as in the  $\text{FeSe}$  binary compound, produces alloys of the type  $(\text{CuInSe}_2)_{1-x}(\text{FeSe})_x$ . For this system, a phase diagram was proposed based on XRD and DTA measurements. At 600 K, two single-phase fields, chalcopyrite and semi-ordered phase, separated by a relatively narrow two-phase field were ob-

TABLE I. Comparative table of crystallographic parameters for  $(\text{CuInSe}_2)_{1-x}(\text{FeSe})_x$  alloys with  $x = 0, 1/3, 1/2, 2/3$ .

$x$	Alloy	SG	$a$ (Å)	$c$ (Å)	$V$ (Å <sup>3</sup> )	Cu-Se (Å)	Fe-Se (Å)	In-Se (Å)	Ref.
0	$\text{CuInSe}_2$	$I\bar{4}2d$	5.781(1)	11.642(3)	389.1(2)	2.432(1)	-	2.591(1)	[21]
1/3	$\text{Cu}_2\text{FeIn}_2\text{Se}_5$	$P\bar{4}2c$	5.7790(2)	11.6093(5)	387.71(3)	2.431(5)	2.458(5)	2.630(5)	[*]
1/2	$\text{CuFeInSe}_3$	$P\bar{4}2c$	5.7762(3)	11.5982(7)	386.97(3)	2.423(8)	2.464(8)	2.602(8)	[10]
2/3	$\text{CuFe}_2\text{InSe}_4$	$I\bar{4}2m$	5.7694(3)	11.495(1)	382.62(4)	2.432(5)	2.488(5)	2.576(5)	[11]

[\*] this work.

TABLE II. SEM experimental results for the sample  $\text{Cu}_2\text{FeIn}_2\text{Se}_5$ .

Composition	MW (g)	Nominal Stoichiometry (%)	Experimental Stoichiometry (%)
$\text{Cu}_2\text{FeIn}_2\text{Se}_5$	807.38	Cu = 20.0 Fe = 10.0 In = 20.0 Se = 50.0	Cu = $20.4 \pm 0.2$ Fe = $09.8 \pm 0.2$ In = $19.9 \pm 0.2$ Se = $49.9 \pm 0.5$

served [12]. These results suggest a phase sequence process as a function of composition ( $x$ ) could be from the ordered chalcopyrite structure  $x = 0$ , to  $x = 1/3$  and  $1/2$  as intermediate disordered phases, before a reordering of the cationic sublattice occurs at values of  $x = 2/3$ . Table I show the crystallographic parameter comparison for the four compositions of the system  $(\text{CuInSe}_2)_{1-x}(\text{FeSe})_x$ . These results suggest that composition  $x = 1/3$ ,  $\text{Cu}_2\text{FeIn}_2\text{Se}_5$ , could crystallize with a disordered structure in its cationic network, however until now its crystalline structure had not been established.

For this reason, to derive a model that explains well all the X-ray diffraction peaks observed in the powder pattern of this compound, a detailed structural analysis of the  $\text{Cu}_2\text{FeIn}_2\text{Se}_5$  alloy using powder X-ray diffraction was performed. The structure of the quaternary  $\text{Cu}_2\text{FeIn}_2\text{Se}_5$  completes the phase transition produced in the  $(\text{CuInSe}_2)_{1-x}(\text{FeSe})_x$  system between the values  $x = 0$  to  $x = 2/3$ .

## 2. Experimental

### 2.1. Synthesis

Starting materials (Cu, Al, Ta, and Se) with nominal purity of 99.99 wt. % in the stoichiometric ratio were mixed in an evacuated ( $10^{-4}$  Torr) and sealed quartz tube with the inner walls previously carbonized to prevent the chemical reaction of the elements with quartz Polycrystalline ingots of about 1 g were prepared by the melting and annealing technique. The quartz ampoule is heated until 493 K (melting point of Se), keeping this temperature for 48 h and shaking all the time using an electromechanical motor. This procedure guarantees the formation of binary species at low temperatures avoiding the existence of Se free gas at high temperature, which could produce explosions or Se deficiency in the ingot. Then

the temperature was slowly increased until 1423 K, with the mechanical shaker always connected for better mixing of the components. After 24 h, the cooling cycle begins until the anneal temperature (800 K) with the mechanical shaker is disconnected. The ampoule is keeping at the annealing temperature for 1 month to assure the thermal equilibrium. Then the furnace is switching off. This preparation method has proven to give good results [6,12].

### 2.2. Scanning Electron Microscopy (SEM)

Stoichiometric relations of the samples were investigated by scanning electron microscopy (SEM) technique, using a Hitachi S2500 equipment. The microchemical composition was found by an energy-dispersive X-ray spectrometer (EDS) coupled with a computer-based multichannel analyzer (MCA, Delta III analysis, and Quantex software, KeveX). For the EDS analysis,  $K_\alpha$  lines were used. The accelerating voltage was 15 kV. The samples were tilted 35 degrees. A standardless EDS analysis was made with a relative error of  $\pm 5-10\%$  and detection limits of the order of 0.3 wt %, where the k-ratios are based on theoretical standards. Table II shows the experimental stoichiometry of the sample  $\text{Cu}_2\text{FeIn}_2\text{Se}_5$ .

### 2.3. Differential Thermal Analysis (DTA)

Differential Thermal Analysis (DTA) measurements were carried out in a fully automatic Perkin-Elmer apparatus, which consists of a Khantal resistance furnace ( $T_{\text{max}} = 1650$  K) equipped with Pt/Pt-Rh thermocouples and an informatics system for the automatic acquisition data. The internal standard used was a high purity (99.99 wt. %) piece of gold. The temperature runs have been performed from ambient temperature to 1400-1500 K, which is the recommended operative limit. The heating rate is controlled electronically to  $20 \text{ K h}^{-1}$ ; the cooling rate was given by the natural cooling of the furnace after switching off. From the thermogram, transition temperatures are manually obtained from the  $\Delta T$  vs.  $T$  graph with the criteria that the transition occurs at the intersection of the baseline with the slope of the thermal transition peak, as usual. The maximum error committed in the determination of transition temperatures by this method is estimated to be  $\pm 10$  K.

## 2.4. X-ray powder diffraction

The X-ray powder diffraction data were collected at room temperature, in a  $\theta/\theta$  reflection mode using a Siemens D5005 diffractometer equipped with an X-ray tube (CuK $\alpha$ 1 radiation:  $\lambda = 1.54056 \text{ \AA}$ ; 40 kV, 30 mA) and a diffracted beam graphite monochromator. A 1 mm aperture slit, a 1 mm divergence slit, a 0.1 mm monochromator slit, and a 0.6 mm detector slit were used. The specimen was scanned in the  $2\theta$  range of  $10 - 110^\circ$ , the scan step was  $0.02^\circ$ , and the time of counting in every step was 10 s. Quartz was used as an external standard. The instrument analytical software was used to establish the positions of the peaks.

## 3. Results and discussion

### 3.1. Differential thermal analysis

In Fig. 1, the thermogram for sample  $\text{Cu}_2\text{FeIn}_2\text{Se}_5$  is displayed.

In the heating cycle, it can be observed two thermal transitions at 1017 and 964 K. The shape of the peak is typical of an incongruent melting point where the solid phase transits to a solid + liquid region at 964 K and then to a liquid phase (melting) at 1017 K. However, in the cooling cycle, up to five thermal transitions are observed. The fact that only two thermal transitions are observed in the heating cycle and five in the cooling is probably due to the difference between the heating and cooling rates in competition with the velocity of the thermal transitions. The heating rate is electronically fixed at 10 K/min, whereas the cooling rate is variable, given by the natural cooling of the furnace after switching off. Transitions solid-to-liquid (and viceversa) are faster than solid-to-solid and involve higher energies (variation in the enthalpy,  $\Delta H$ ), for these reasons, solid-to-solid transitions are better observed in the cooling cycle.

The high-temperature transition at 1366 K in the cooling, coincides with the melting point of FeSe reported as 1348 K [22] suggesting that, at this temperature, the liquid phase un-

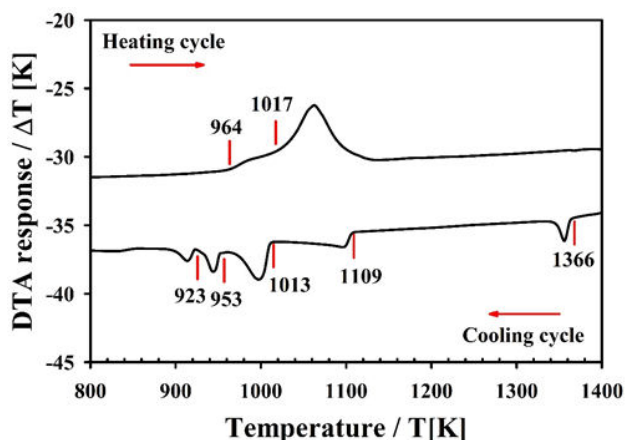


FIGURE 1. DTA response of sample  $\text{Cu}_2\text{FeIn}_2\text{Se}_5$ .

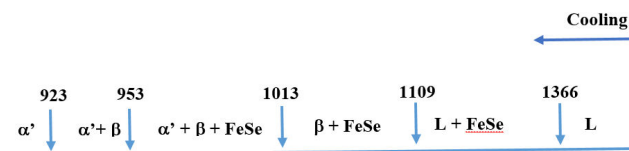


FIGURE 2. Schematic illustration of thermal transitions for the sample  $\text{Cu}_2\text{FeIn}_2\text{Se}_5$  in the cooling cycle.

dergoes to a liquid + FeSe region. The liquid + FeSe region is wide, from 1366 K to 1109 K (257 degrees). At 1109 K, the liquid phase solidifies, possibly in the disordered sphalerite  $\beta$ -phase accompanied by FeSe-phase. At 1013 K, the semi-ordered  $\alpha'$ -phase coexists with the  $\beta'$ -phase and FeSe, at 953 K, the region is  $\alpha' + \beta$  and finally, at 923 K, the region is only  $\alpha'$ . In Fig. 2, a schematic representation of the successive phase transitions is given.

### 3.2. X-ray powder diffraction analysis

Figure 3 shows the resulting X-ray powder pattern for the  $\text{Cu}_2\text{FeIn}_2\text{Se}_5$  compound. When the  $2\theta$  positions of the 20 first peaks in the diffraction pattern are introduced into the auto-indexing program Dicvol04 [23], a tetragonal cell of dimensions  $a = 5.780(1) \text{ \AA}$ ,  $c = 11.610(2) \text{ \AA}$  is obtained. These parameters are similar in magnitude to the parent's chalcopyrite structure  $\text{CuInSe}_2$  [21] and  $P$ -chalcopyrite structure  $\text{CuFeInSe}_3$  [10]. The systematic absence condition in the general reflections of the type  $hkl$  indicating a  $P$ -type cell, and the  $hhl : l = 2n$  and  $00l : l = 2n$  conditions suggests the extension symbol  $P\bar{4}2c$ . To find the atomic positions to adjust the diffraction pattern was employed a similar analysis to that used in the structural determination of the quaternary alloy  $\text{CuFeInSe}_3$ , which crystallize in the same space group [10]. It should be noted that this analysis was carried out starting from the prototype of the  $P$ -chalcopyrite structure, which was the structure of the Cu-poor Cu-In-Se compound  $\beta\text{-Cu}_{0.39}\text{In}_{1.2}\text{Se}_2$  [24].

Table III shows the 6 better models used in the cation distribution analysis on the available Wyckoff positions. In this

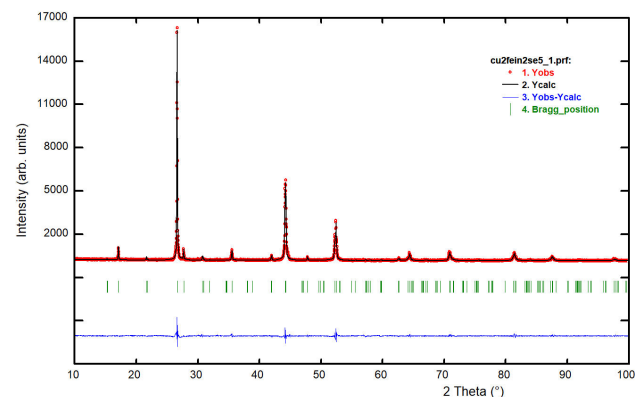


FIGURE 3. A plot illustrating the final Rietveld refinement of  $\text{Cu}_2\text{FeIn}_2\text{Se}_5$ . The bars in the graphic symbolize the Bragg peak positions. The lower trace is the difference curve between observed and calculated patterns.

TABLE III. Cation distribution models in the Rietveld refinement of the quaternary alloy  $\text{Cu}_2\text{FeIn}_2\text{Se}_5$ .

Model	(2e)	(2a)	(2b)	(2c)	(2d)	(2f)	(8n)	$R_p$	$R_{wp}$	S
	0,0,0	0,0,1/4	1/2,0,1/4	1/2,1/2,1/4	0,1/2,1/4	1/2,1/2,0	$x, y, z$			
1	Cu1	-	Fe1	-	In1	M	Se	11.0	16.3	2.6
2	Cu1	-	Fe1	-	M	In1	Se	11.2	15.9	2.6
3	Cu1	-	In1	-	Fe1	M	Se	7.8	8.8	1.4
4	Cu1	-	In1	-	M	Fe1	Se	11.4	17.1	2.8
5	Cu1	-	M	-	Fe1	In1	Se	30.6	41.2	6.6
6	Cu1	-	M	-	In1	Fe1	Se	29.4	40.1	6.5

Fe1 (cation) (foc= 0.8Fe+0.1Cu2+0.1In2); M = (Cu3+In3) (foc= 0.5), (foc= 0.5); Se (anion) : ( $x \approx 1/4, y \approx 1/4, z \approx 1/8$ ).

Table the Rietveld refinement [25] results are shown. Many other tests were performed where the  $\text{Cu}^+$  cations were moved from the origin (2e), and Wyckoff positions (2a) and (2c) were used for the cations distribution, but only with poor results. The final model was confirmed by checking the chemical sense of the structure in terms of its distances and bond angles.

The program Fullprof [26] was employed for the Rietveld refinement analyzes. In each case, the angular dependence was described by the usual constrain imposed by the Cagliotti's formula [27], and the peak shapes were described by the Thompson-Cox-Hastings pseudo-Voigt profile function [28]. The background was described by the automatic interpolation of 67 points throughout the whole pattern. One overall isotropic temperature factor was refined to describe the thermal motion of the atoms. Model 3 showed the best fit and the Rietveld refinement results are shown in Table IV. Figure 3 shows the Rietveld refinement plot for the quaternary compound  $\text{Cu}_2\text{FeIn}_2\text{Se}_5$ . Table V shows the atomic coordinates, isotropic temperature factor, bond distances, and angles for the new compound.

$\text{Cu}_2\text{FeIn}_2\text{Se}_5$  is a normal adamantane structure compound [5], and consists of a three-dimensional arrangement

of distorted  $\text{CuSe}_4$ ,  $\text{FeSe}_4$  and  $\text{InSe}_4$  tetrahedral connected by common faces (Fig. 4b). In this compound, as in the related  $\text{CuFeInSe}_3$ , occurs a degradation of symmetry from the chalcopyrite structure  $I\bar{4}2d$  to a related structure  $P\bar{4}2c$  [10]. In this adamantane model, each cation is tetrahedrally bonded to four anions and at the same time, each Se anion is coordinated by four cations [one Cu1, one Fe, one In1, and one M cation (either Cu2 or In2)] located at the corners of a lightly distorted tetrahedron.

The tetrahedra containing the Cu1 atoms [mean Se...Se distance 3.970(6) Å] are lightly smaller than those containing the M (Cu2 or In2) [means Se...Se distance 4.108(6) Å], Fe atoms [mean Se...Se distance 4.012(6) Å], and In1 atoms [mean Se...Se distance 4.294(6) Å] respectively.

The interatomic distances are shorter than the sum of the respective ionic radii for structures tetrahedrally bonded [29]. The Cu-Se [2.431(5) Å], Fe-Se [2.458(5) Å] and In-Se [2.630(5) Å], bond distances compare well to those observed in some other adamantane structure compounds such as  $\text{CuInSe}_2$  (2.432–2.591 Å) [21],  $\text{Cu}_2\text{SnSe}_3$  (2.415 Å) [30],  $\text{CuFeInSe}_3$  (2.421–2.520 Å) [10],  $\text{CuFe}_2\text{InSe}_4$  (2.417–2.50 Å) [11],  $\text{CuMn}_2\text{InSe}_4$  (2.447–2.594 Å) [31],  $\text{CuMnInSe}_3$

TABLE IV. Rietveld refinement results for  $\text{Cu}_2\text{FeIn}_2\text{Se}_5$ .

Molecular formula	$\text{Cu}_2\text{FeIn}_2\text{Se}_5$	wavelength (CuK $\alpha$ )	1.54056 Å
Molecular weight (g/mol)	807.38	data range $2\theta$ (°)	10-100
$a$ (Å)	5.7790(2)	step size $2\theta$ (°)	0.02
$c$ (Å)	11.6093(8)	counting time (s)	40
$c/a$	2.00	step intensities	4501
$V$ (Å <sup>3</sup> )	387.71(3)	independent reflections	152
$Z$	1.6 (8/5)	$R_p$ (%)	7.8
Crystal system	tetragonal	$R_{wp}$ (%)	8.8
Space group	$P\bar{4}2c$ (N° 112)	$R_{exp}$ (%)	6.2
$d_{calc}$ (g/cm <sup>-3</sup> )	5.55	$R_B$ (%)	7.0
Temperature (K)	298(1)	S	1.4

$R_{exp} = 100[(N - P + C) / \sum_w (y_{obs}^2)]^{1/2}$   $R_p = 100 \sum |y_{obs} - y_{calc}| / \sum |y_{obs}|$   $R_{wp} = 100[\sum_w |y_{obs} - y_{calc}|^2 / \sum_w |y_{obs}|^2]^{1/2}$   $S = [R_{wp} / R_{exp}]$   $R_B = 100 \sum_k |I_k - I_{c_k}| / \sum_k |I_k|$   $N - P + C$  is the number of degrees of freedom

TABLE V. Atomic coordinates, occupancy factors, isotropic temperature factors, bond, and angle distances for  $\text{Cu}_2\text{FeIn}_2\text{Se}_5$ , derived from the Rietveld refinement.

Atom	Ox.	Wyck.	$x$	$y$	$z$	foc	B ( $\text{\AA}^2$ )	
Cu1	+1	2e	0	0	0	1	0.51(5)	
Fe	+2	2d	0	1/2	1/4	0.8	0.51(5)	
Cu2	+1	2d	0	1/2	1/4	0.1	0.51(5)	
In2	+3	2d	0	1/2	1/4	0.1	0.51(5)	
In1	+3	2b	1/2	0	1/4	1	0.51(5)	
Cu3	+1	2f	1/2	1/2	0	0.5	0.51(5)	
In3	+3	2f	1/2	1/2	0	0.5	0.51(5)	
Te	-2	8n	0.2306(7)	0.2568(7)	0.1197(5)	1	0.51(5)	
Cu1-Se		2.431(5)	Fe1-Se		2.458(5)	In1-Sei		2.630(5)
Se <sup>ii</sup> -Cu1-Se		109.1(2) x 4	Se <sup>ii</sup> -Cu1-Se <sup>iii</sup>		110.3(1) x 2	Se-Fe-Seiv		114.3(2) x 4
Se <sup>vi</sup> -In1-Se <sup>i</sup>		111.3(1) x 2	Se <sup>v</sup> -In1-Se <sup>ii</sup>		109.8(1) x 2	Se-Fe-Sev		104.0(1) x 2
Se <sup>vi</sup> -In1-Se		107.4(1) x 2	Se <sup>viii</sup> -M-Se		107.8(2) x 4	Seviii-M-Seix		113.0(1) x 2

Symmetry codes: (i)  $1-x, -y, z$ ; (ii)  $-y, x, -z$ ; (iii)  $y, -x, -z$ ; (iv)  $x, 1-y, 0.5-z$ ; (v)  $-x, 1-y, z$ ; (vi)  $x, -y, 0.5-z$ ; (vii)  $1-x, y, 0.5-z$ ; (viii)  $y, 1-x, -z$ ; (ix)  $1-y, x, -z$ .

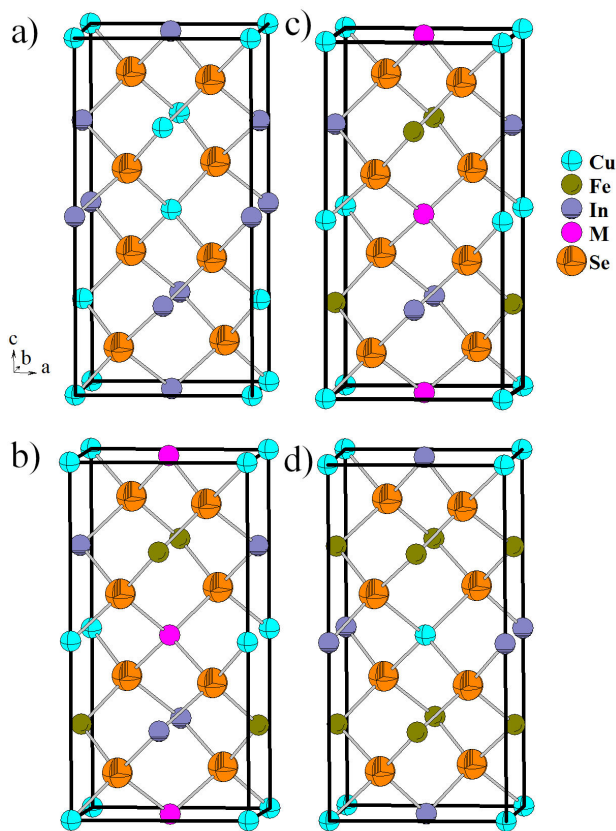


FIGURE 4. a)  $\text{CuInSe}_2$  ( $I\bar{4}2d$ ), b)  $\text{Cu}_2\text{FeIn}_2\text{Se}_5$  ( $P\bar{4}2c$ ) c)  $\text{CuFeInSe}_3$  ( $P\bar{4}2c$ ) d)  $\text{CuFe}_2\text{InSe}_4$  ( $I\bar{4}2m$ ) Unit cell diagram, in the  $ca$  plane, for the chalcopyrite a)  $\text{CuInSe}_2$  ( $I\bar{4}2d$ ) ( $x = 0$ ), compared with the P-chalcopyrite structures ( $P\bar{4}2c$ ) b)  $\text{Cu}_2\text{FeIn}_2\text{Se}_5$  ( $x = 1/3$ ) and c)  $\text{CuFeInSe}_3$  ( $x = 1/2$ ), and the stannite structure d)  $\text{CuFe}_2\text{InSe}_4$  ( $I\bar{4}2m$ ) ( $x = 2/3$ ).

(2.428 – 2.614  $\text{\AA}$ ) [13],  $\text{CuVInSe}_3$  (2.518 – 2.530  $\text{\AA}$ ) [32] and  $\text{Cu}_3\text{In}_7\text{Se}_{12}$  (2.419 – 2.523  $\text{\AA}$ ) [33].

The chemical structural model was checked by the analysis of the interatomic distances using the BVS formula based on the bond-strength examination [34,35]. The atomic valence of an atom is assumed to be distributed between the bonds that it forms. BVS of atom  $i$ , denoted  $V_i$ , is then  $V_i = \sum_j S_j = \sum_j \exp[(R_o - R_{ij})/b]$ , where  $S_j$  is the valence of one bond, and the sum is over all neighbors  $j$ . The constant  $b = 0.37$  was empirically determined [34].  $R_o$  represents the length of a bond of a unit valence, and  $R_{ij}$  is the experimentally determined distance between atoms  $i$  and  $j$ . The values for the reference distance  $R_o$  for Cu-Se, Fe-Se, and In-Se are 2.02, 2.28 and 2.47  $\text{\AA}$ , respectively [35]. Table VI shows the BVS results for  $\text{Cu}_2\text{FeIn}_2\text{Se}_5$ , indicating that the oxidation state for each ion is in good agreement with the expected formal oxidation state of  $\text{Cu}^+$ ,  $\text{Fe}^{2+}$ ,  $\text{In}^{3+}$ , and  $\text{Se}^{2-}$  ions.

Figure 4 shows the crystal structure evolution of  $(\text{CuInSe}_2)_{1-x}(\text{FeSe})_x$  alloys, which confirms the phase diagram proposed for this system [12]. Starting from the chalcopyrite structure (Fig. 4a)  $\text{CuInSe}_2$  with space group  $I\bar{4}2d$ ,

TABLE VI. Bond Valence Sum (BVS) calculations for  $\text{Cu}_2\text{FeIn}_2\text{Se}_5$ .

	Cu	Fe	In	M	Se
$V_i$	1.4	2.3	3.1	1.9	2.2
formal					
oxidation state	1	2	3	2	2

$V_i = \sum_j \exp[(R_o - R_{ij})/b]$ ;  $b = 0.37 \text{ \AA}$ ;  $R_o$  (Cu-Se) = 2.02  $\text{\AA}$ ;  $R_o$  (Fe-Se) = 2.28  $\text{\AA}$ ;  $R_o$  (In-Se) = 2.47  $\text{\AA}$ .

when introducing a transition metal (Fe) into the chalcopyrite matrix, a first effect is the disorder of the cationic network. This effect is observed in the *P*-chalcopyrite structures with (Fig. 4b)  $x = 1/3$   $\text{Cu}_2\text{FeIn}_2\text{Se}_5$  (this work) and (Fig. 4c)  $x = 1/2$   $\text{CuFeInSe}_3$ , both crystallize in space group  $P\bar{4}2c$ , where a cationic disorder resulting from the occupation of several cations in the same Wyckoff site is observed. By increasing the amount of the transition metal to  $x = 2/3$ , the cationic network is reordered in a tetragonal space group  $I\bar{4}2m$   $\text{CuFe}_2\text{InSe}_4$  (Fig. 4d), which crystallize with a stannite-type structure.

From the magnetic point of view, these materials—due to their cationic ordering—are diamagnetic, ferromagnetic, and ferromagnetic, respectively [6,12].

#### 4. Conclusions

A new quaternary chalcogenide, belonging to the system  $(\text{CuInSe}_2)_{1-x}(\text{FeSe})_x$  with  $x = 1/3$ , has been synthesized

and structurally characterized. The DTA indicates that this compound melts at 1017 K. The crystal structure solution of the semiconductor alloy  $\text{Cu}_2\text{FeIn}_2\text{Se}_5$  was resolved in the space group  $P\bar{4}2c$  by the evaluation of different models derived from the  $\text{CuFeInSe}_3$  structure against the powder X-ray diffraction data, using the Rietveld method. This compound crystallizes in a *P*-chalcopyrite structure and is the first structural report on a member of the  $\text{I}_2\text{-II-III}_2\text{-VI}_5$  semiconductor composition. Its structure completes the phase transition produced in the  $(\text{CuInSe}_2)_{1-x}(\text{FeSe})_x$  system between the values  $x = 0$  to  $x = 2/3$ .

#### Acknowledgments

This work was partially done into G.E. Delgado visit at the Universidad de Antofagasta, supported by MINEDUC-UA project, code ANT 1856.

1. J. L. Shay and J. H. Wernick, *Ternary Chalcopyrite Semiconductors: Growth Electronic Properties, and Applications* (Pergamon Press, Oxford, 1975), <https://doi.org/10.1016/C2013-0-02602-3>.
2. B. R. Pamplin, T. Kiyosawa, and K. Masumoto, Ternary chalcopyrite compounds, *Prog. Cryst. Growth Charact.* **1** (1979) 331, [https://doi.org/10.1016/0146-3535\(79\)90002-9](https://doi.org/10.1016/0146-3535(79)90002-9).
3. J. E. Jaffe and A. Zunger, Theory of the band-gap anomaly in AB  $C_2$  chalcopyrite semiconductors, *Phys. Rev. B* **29** (1984) 1882, <https://doi.org/10.1103/PhysRevB.29.1882>.
4. L. Pauling and L. O. Brockway, The Crystal Structure of Chalcopyrite  $\text{CuFeS}_2$ , *Z. Kristall.* **82** (1932) 188, <https://doi.org/10.1524/zkri.1932.82.1.188>.
5. E. Parthé, Wurzite and Sphalerite Structures, in *Intermetallic Compounds*, edited by J. H. Westbrook and R. L. Fleischer, Vol. 1 (Wiley, Chichester, 1995).
6. P. Grima-Gallardo *et al.*, A comparative Study of  $(\text{Cu-III-Se}_2)_x\text{-(FeSe)}_{1-x}$  Alloys (III: Al, Ga, In) ( $0 \leq x \leq 1$ ) by X-Ray Diffraction, Differential Thermal Analysis and Scanning Electron Microscopy, *Phys. Status Solidi A* **187** (2001) 395, [https://doi.org/10.1002/1521-396X\(200110\)187:2<395::AID-PSSA395>3.0.CO;2-2](https://doi.org/10.1002/1521-396X(200110)187:2<395::AID-PSSA395>3.0.CO;2-2).
7. P. Grima-Gallardo *et al.*, X-Ray Diffraction (XRD), Differential Thermal Analysis (DTA), and Scanning Electron Microscopy (SEM) of  $(\text{CuInSe}_2)_{1-x}(\text{VSe})_x$  Alloys ( $0 \leq x \leq 0.5$ ), *Phys. Status Solidi A* **193** (2002) 217, [https://doi.org/10.1002/1521-396X\(200209\)193:2<217::AID-PSSA217>3.0.CO;2-O](https://doi.org/10.1002/1521-396X(200209)193:2<217::AID-PSSA217>3.0.CO;2-O).
8. P. Grima-Gallardo *et al.*, The  $(\text{CuGaSe}_2)_{1-x}(\text{MgSe})_x$  alloy system ( $0 \leq x \leq 0.5$ ): X-ray diffraction, energy dispersive spectrometry and differential thermal analysis, *Phys. Status Solidi B* **241** (2004) 1789, <https://doi.org/10.1002/pssb.200302010>.
9. P. Grima-Gallardo *et al.*, Preparation and investigation  $(\text{Cu-III-Se}_2)_{1-x}(\text{NbSe})_x$  alloys (III: Ga, In) with  $x = 1/2$ , *Phys. Status Solidi A* **204** (2007) 1093, <https://doi.org/10.1002/pssa.200622568>.
10. A. J. Mora, G. E. Delgado, and P. Grima-Gallardo, Crystal structure of  $\text{CuFeInSe}_3$  from X-ray powder diffraction data, *Phys. Status Solidi A* **204** (2007) 547, <https://doi.org/10.1002/pssa.200622395>.
11. G. E. Delgado, A. J. Mora, P. Grima-Gallardo, and M. Quintero, Crystal structure of  $\text{CuFe}_2\text{InSe}_4$  from X-ray powder diffraction, *J. Alloys Compd.* **454** (2008) 306, <https://doi.org/10.1016/j.jallcom.2006.12.057>.
12. P. Grima-Gallardo *et al.*, Phase Diagram of  $(\text{CuInSe}_2)_{1-x}(\text{FeSe})_x$  alloys, *J. Alloys Compd.* **630** (2015) 146, <https://doi.org/10.1016/j.jallcom.2015.01.015>.
13. G. E. Delgado, J. A. Flores-Cruz, P. Grima-Gallardo, M. Quintero, and A. Moreno, Synthesis and Crystal Structure of Three New Quaternary Compounds in the system Cu- Mn-III-Se<sub>3</sub> (III = Al, Ga, In), *Mater. Res.* **21** (2018) e20160748, <https://doi.org/10.1590/1980-5373-mr-2016-0748>.
14. G. M. Ford, Q. Guo, R. Agrawal, and H. W. Hillhouse, Earth Abundant Element  $\text{Cu}_2\text{Zn}(\text{Sn}_{1-x}\text{Ge}_x)\text{S}_4$  Nanocrystals for Tunable Band Gap Solar Cells: 6.8% Efficient Device Fabrication, *Chem. Mater.* **23** (2011) 2626, <https://doi.org/10.1021/cm2002836>.
15. Q. Guo *et al.*, Fabrication of 7.2% Efficient CZTSSe Solar Cells Using CZTS Nanocrystals, *J. Am. Chem. Soc.* **132** (2010) 17384, <https://doi.org/10.1021/ja108427b>.
16. Y. Li *et al.*, Electronic, optical and lattice dynamic properties of the novel diamond-like semiconductors  $\text{Li}_2\text{CdGeS}_4$  and

- $\text{Li}_2\text{CdSnS}_4$ , *J. Phys. Condens. Matter* **23** (2011) 225401, <https://doi.org/10.1088/0953-8984/23/22/225401>.
17. H. Cabrera *et al.*, Thermoelectric transport properties of  $\text{CuFeInTe}_3$ , *J. Alloys Compd.* **651** (2015) 490, <https://doi.org/10.1016/j.jallcom.2015.08.128>.
  18. S. A. Chambers and Y. K. Yoo, New Materials for Spintronics, *MRS Bull.* **28** (2003) 706, <https://doi.org/10.1557/mrs2003.210>.
  19. P. Grima-Gallardo *et al.*, Superparamagnetism in  $\text{CuFeInTe}_3$  and  $\text{CuFeGaTe}_3$  alloys, *Phys. Status Solidi A* **209** (2012) 1141, <https://doi.org/10.1002/pssa.201127663>.
  20. J. Parkes, R. D. Tomlinson, and M. J. Hampshire, Crystal data for  $\text{CuInSe}_2$ , *J. Appl. Cryst.* **6** (1973) 414, <https://doi.org/10.1107/S0021889873009027>.
  21. K. S. Knight, The crystal structures of  $\text{CuInSe}_2$  and  $\text{CuInTe}_2$ , *Mater. Res. Bull.* **27** (1992) 161, [https://doi.org/10.1016/0025-5408\(92\)90209-I](https://doi.org/10.1016/0025-5408(92)90209-I).
  22. H. Okamoto, The fese (iron-selenium) system, *J. Ph. Equilibria* **12** (1991) 383, <https://doi.org/10.1007/BF02649932>.
  23. A. Boulouf and D. Louër, Powder pattern indexing with the dichotomy method, *J. Appl. Cryst.* **37** (2004) 724, <https://doi.org/10.1107/S0021889804014876>.
  24. W. Hönle, F. Kühn, and U.-C. Boehnke, Crystal structures of two quenched Cu-In-Se phases, *Cryst. Res. Technol.* **23** (1988) 1347, <https://doi.org/10.1002/crat.2170231027>.
  25. H. M. Rietveld, A profile refinement method for nuclear and magnetic structures, *J. Appl. Cryst.* **2** (1969) 65, <https://doi.org/10.1107/S0021889869006558>.
  26. J. Rodríguez-Carvajal, *Fullprof ver. 7.3, Laboratoire Léon Brillouin* (CEA-CNRS), France (2020).
  27. G. Caglioti, A. Paoletti, and F. P. Ricci, Choice of collimators for a crystal spectrometer for neutron diffraction, *Nucl. Instrum.* **3** (1958) 223, [https://doi.org/10.1016/0369-643X\(58\)90029-X](https://doi.org/10.1016/0369-643X(58)90029-X).
  28. P. Thompson, D. E. Cox, and J. B. Hastings, Rietveld refinement of Debye-Scherrer synchrotron X-ray data from  $\text{Al}_2\text{O}_3$ , *J. Appl. Cryst.* **20** (1987) 79, <https://doi.org/10.1107/S0021889887087090>.
  29. R. D. Shannon, Revised effective ionic radii and systematic studies of interatomic distances in halides and chalcogenides, *Acta Cryst. A* **32** (1976) 751, <https://doi.org/10.1107/S0567739476001551>.
  30. G. E. Delgado, A. J. Mora, G. Marcano, and C. Rincón, Crystal structure refinement of the semiconducting compound  $\text{Cu}_2\text{SnSe}_3$  from X-ray powder diffraction data, *Mater. Res. Bull.* **38** (2003) 1949, <https://doi.org/10.1016/j.materresbull.2003.09.017>.
  31. G. E. Delgado and V. Sagredo, Crystal structure of the new diamond-like semiconductor  $\text{CuMn}_2\text{InSe}_4$ , *Bull. Mater. Sci.* **39** (2016) 1631, <https://doi.org/10.1007/s12034-016-1323-7>.
  32. G. Marroquín, G. E. Delgado, P. Grima-Gallardo, and M. Quintero, Preparation, differential thermal analysis and crystal structure of the new quaternary compound  $\text{CuVInSe}_3$ , *Rev. Mex. Fis.* **64** (2018) 548, <https://doi.org/10.31349/RevMexFis.64.548>.
  33. G. E. Delgado, L. Manfredy, and S. A. López-Rivera, Crystal structure of the ternary semiconductor  $\text{Cu}_2\text{In}_{14/3}\text{□}_{4/3}\text{Se}_8$  determined by X-ray powder diffraction data, *Powder Diffr.* **33** (2018) 237, <https://doi.org/10.1017/S0885715618000519>.
  34. I. D. Brown and D. Altermatt, Bond-valence parameters obtained from a systematic analysis of the Inorganic Crystal Structure Database, *Acta Cryst. B* **41** (1985) 244, <https://doi.org/10.1107/S0108768185002063>.
  35. N. E. Brese and M. O'Keeffe, Bond-valence parameters for solids, *Acta Cryst. B* **47** (1991) 192, <https://doi.org/10.1107/S0108768190011041>.